Supporting Information for

Hot Electron-Driven Nitrate-to-Ammonia Conversion on Nanocatalyst: Insights from Quantum Dynamics Simulations

*Ankita Kumari[1], Sergei Tretiak[2,3] *, Dibyajyoti Ghosh[1,4] **

[1]Department of Chemistry, Indian Institute of Technology, Delhi, Hauz Khas, New Delhi-110016, India

[2] Center for Integrated Nanotechnologies and Center for Nonlinear Studies, Los Alamos National Laboratory, Los Alamos, NM 87545, USA

[3]Theoretical Division, Los Alamos National Laboratory, Los Alamos, NM 87545, USA

[4] Department of Materials Science and Engineering (DMSE), Indian Institute of Technology, Delhi, Hauz Khas, New Delhi-110016, India

Section S1: Static Structural Details

In our study, we model -Cl passivated $Cd_{28}Se_{17}$ quantum dot (QD) with an average diameter of 1.2 nm, as shown in Figure 1a. The average Cd-Cl bond length is calculated to be 2.62 Å, while the core Cd-Se bond lengths (angles) are in the range of 2.64-2.67 Å (109.3-109.6°), consistent with previous computational studies.[1] The partial density of states (pDOS) plot reveals that Se (p) orbitals mainly dominate the valence band maximum (VBM), while the conduction band minimum (CBM) is mainly dominated by Cd (s) orbitals.

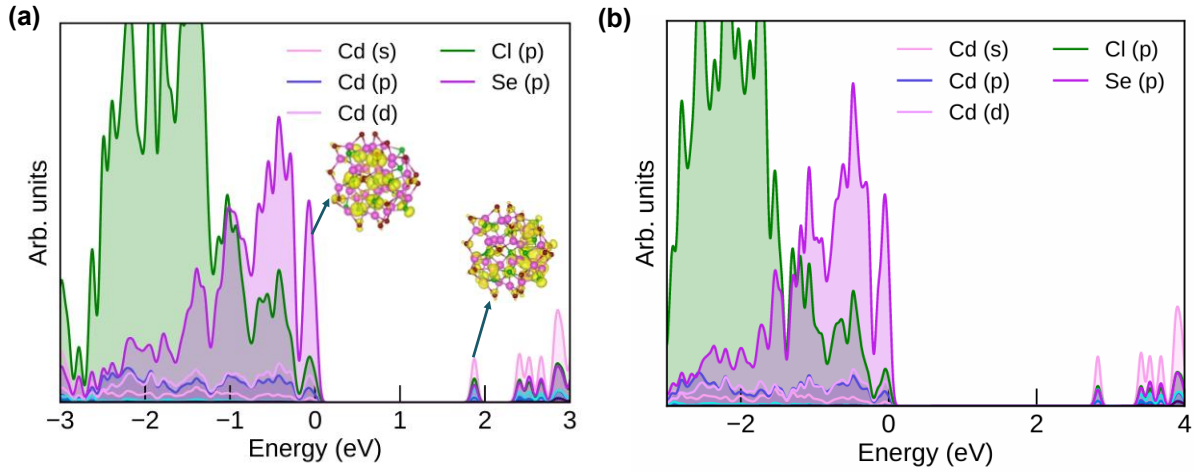

Figure S1: *The electronic partial density of states of -Cl passivated $Cd_{28}Se_{17}$ QD calculated using* ***(a)*** *PBE-GGA functional and* ***(b)*** *range-separated hybrid functional (HSE06). The inset in (a) shows charge densities at VBM and CBM states.*

Section S2: Static Structural and Electronic Details:

The $Cd_{28}Se_{17}Cl_{22}$ QD features five exposed uncoordinated Cd sites (Cd_{3c}), which serve as potential active sites for molecular adsorption. We strategically adsorbed two nitrate (NO_3^-) molecules onto two opposed Cd_{3c} centers to maintain computation tractability and ensure the system has no net dipole moment. This symmetric configuration minimizes polarization effects and more accurately represents the local adsorption environment on the QD surface. While the total system remains globally neutral, chemical notation (NO_3^- and Cd^{2+}) reflects the effective local charge states that govern the adsorbate-surface interactions. Such Cd-rich surfaces

function analogously to sorbents in water purification technologies, where negatively charged NO_3^- binds to electropositive centers. The adsorbate preferentially binds through the O-site with an average Cd-O bond length in the range of 2.34Å. The optimized geometry shows that one of the NO_3^- molecules binds to two neighboring Cd_{3c} sites. The other NO_3^- binds to the Cd^{+2} site where two O atoms anchor to a single Cd^{+2} center, forming $Cd(NO_3)_2$-like species. These configurations reflect the electrostatic interaction between the negatively charged NO_3^- ions and the locally electropositive Cd^{2+} centers on the QD surface, akin to anion binding in aqueous sorbent systems.

To further investigate the electronic properties of QD-NO_3, we compute the density of states (DOS) using both PBE and range-separated hybrid functionals. These calculations provide key insights into electronic structure and molecular state alignment within the QD-adsorbate system. Figure 1c and S2 show that the projected DOS reveals molecular state contribution just above the CBM. The LUMO state of the other NO_3 remains deeper within the conduction band (~2.0 eV), suggesting its limited influence in near band-edge photoexcitation-induced charge carrier dynamics. Thus, the adsorbate-adsorbent binding geometry strongly impacts the energetic alignments of the molecular states of the adsorbate with the electronic bands of the sorbent.[2]

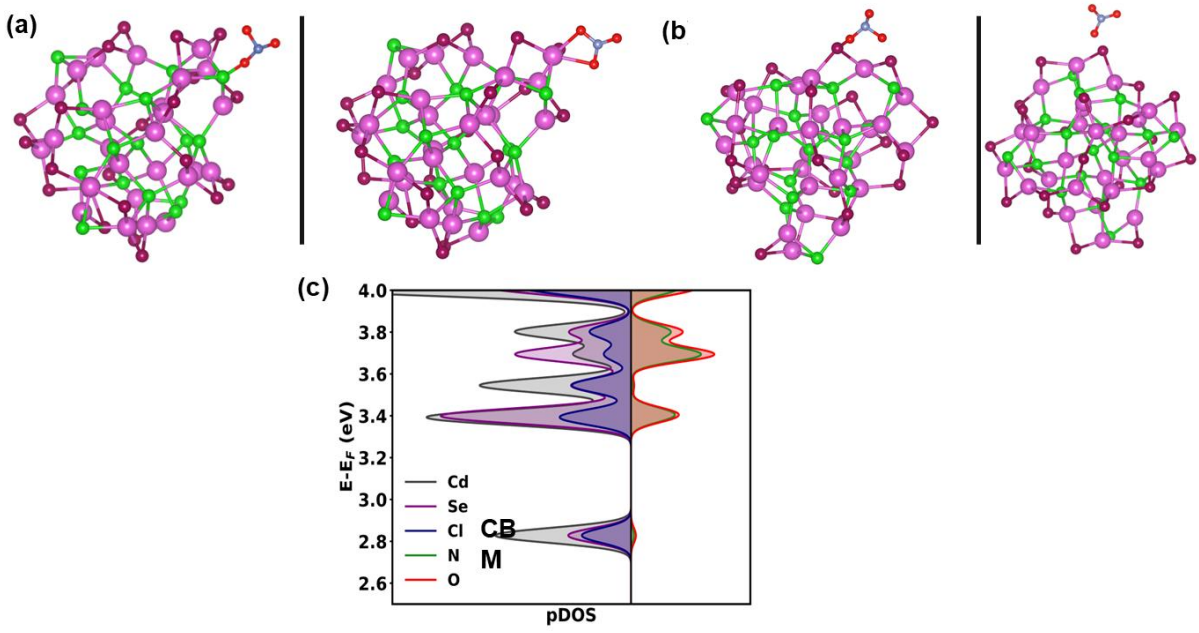

Figure S2: (a) *Unoptimized geometry (left panel) of NO_3^- species adsorbed on the Se-top site of the $Cd_{28}Se_{17}Cl_{22}$ QD, and the right panel shows the optimized geometry of the same system.* ***(b)*** *Unoptimized geometry (left panel) of NO_3^- species adsorbed on the Cl-top site of the $Cd_{28}Se_{17}Cl_{22}$ QD, and the right panel shows the optimized geometry of the same system.* ***(c)***

The pDOS plot of the conduction band states of the QD-NO_3 system using range-separated hybrid functionals (HSE06).

Section S3: Solvent Effect

We employed VASPsol, a software package integrating solvation effects within VASP using a self-consistent continuum model for implicit solvation calculations.[3] VASPsol has gained popularity recently due to its computational efficiency and simplicity, making it a valuable tool for studying various heterogeneous catalysis systems.[4,5] In this approach, the total energy obtained from DFT is supplemented by contributions from electrostatic interactions between the solute and solvent and the cavitation energy required to form the solute within the solvent environment. The following equation gives the expression for E_{elec} and E_{cav}:

$$E_{cav} = \tau \int d\vec{r}\, |\nabla S(\vec{r})| \quad (1)$$

$$E_{elec} = -\int d\vec{r}\, \varepsilon(\vec{r}) \frac{|\nabla \phi(\vec{r})|^2}{8\pi} \quad (2)$$

where, $\varepsilon(\vec{r})$ represents the solvent dielectric constant, $S(\vec{r})$ is the cavity shape function, $\phi(\vec{r})$ is the total electrostatic potential, and τ is the surface tension. The dielectric constant and cavity shape function are given by:

$$\boldsymbol{\varepsilon}\big(n_{\text{solute}}(\vec{r})\big) = 1 + (\varepsilon_b - 1) S\big(n_{\text{solute}}(\vec{r})\big) \quad (3)$$

$$S(r) = \frac{1}{2}\,\text{erfc}\left\{\frac{\ln(\rho(r)/\rho_c)}{\sigma\sqrt{2}}\right\} \quad (4)$$

where ρ is the electron density, ρ_c is the cutoff electron density, and σ defines the cavity width. Our simulations employ solvent-specific dielectric constants to account for the varying polarities of different solvents. The dielectric constants used are 78.35 for water, 2.37 for toluene, and 24.85 for ethanol, ensuring a realistic representation of the solvation environment (Figure S3a-c).In addition to the dielectric constant, other implicit solvation parameters in VASPsol are set to standard values. The cavity width σ is fixed at 0.6 Å, while the cutoff electron density $\rho_c$is maintained at 0.0025 $Å^{-3}$. Furthermore, a surface tension parameter τ 0.525 meV/$Å^2$ accounts for the energy associated with cavity formation in the solvent. These parameters collectively ensure a consistent and accurate description of solvation effects in the $Cd_{28}Se_{17}Cl_{22}$ QD-NO_3 system. As shown in Figure S3a-c, the NO_3 molecular states in the QD-NO_3 system remain largely unaffected under polar (water, ethanol) and non-polar (toluene) solvents, with minimal energy shifts of ~0.23-0.25 eV. The NO_3^- adsorption energies in polar

(water, ethanol) and non-polar (toluene) solvents are in the range -2.33 to -2.35 eV, which remain close to the corresponding value computed considering the gas phase (-2.11 eV). This modest stabilization suggests that solvation does not influence the overall adsorption energetics substantially. Since solvation effects do not significantly influence the electronic properties of QD-NO_3, we adopt a gas-phase model for the remainder of the computational study.

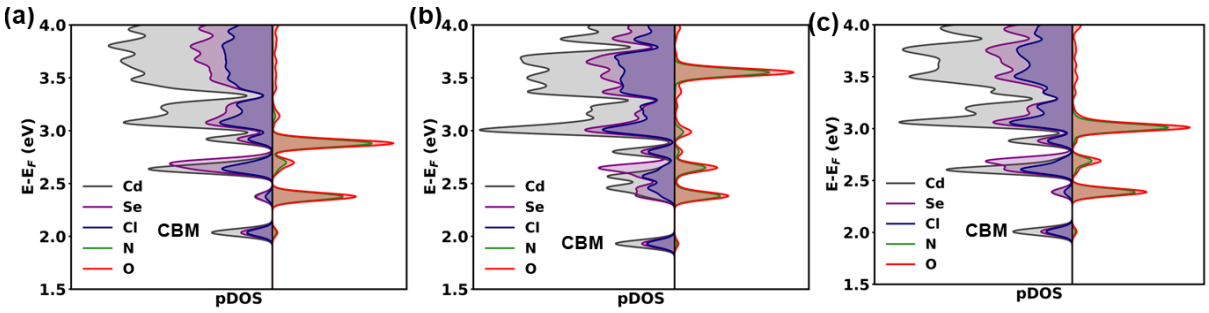

Figure S3: *The electronic projected density of states (pDOS) at the conduction band edge considering solvent* ***(a)*** *water,* ***(b)*** *toluene, and* ***(c)*** *ethanol. The QD states are on the left, while the molecular LUMO states in QD-NO_3 appear on the right.*

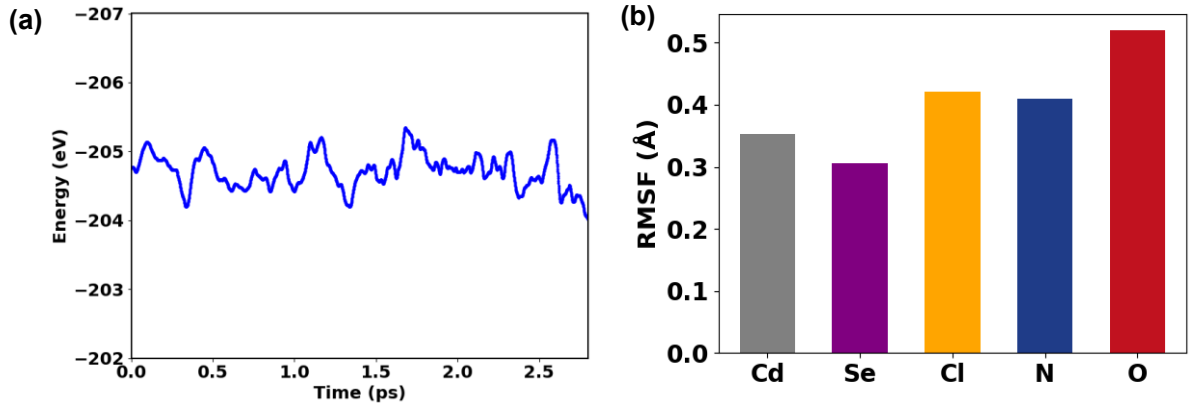

Figure S4:(a) *Potential energy curve for QD-NO_3 system demonstrating equilibration at 300K for conducted AIMD simulations.* ***(b)*** *The root mean square fluctuations of individual elements of the $Cd_{28}Se_{17}Cl_{22}$-NO_3 QD system.*

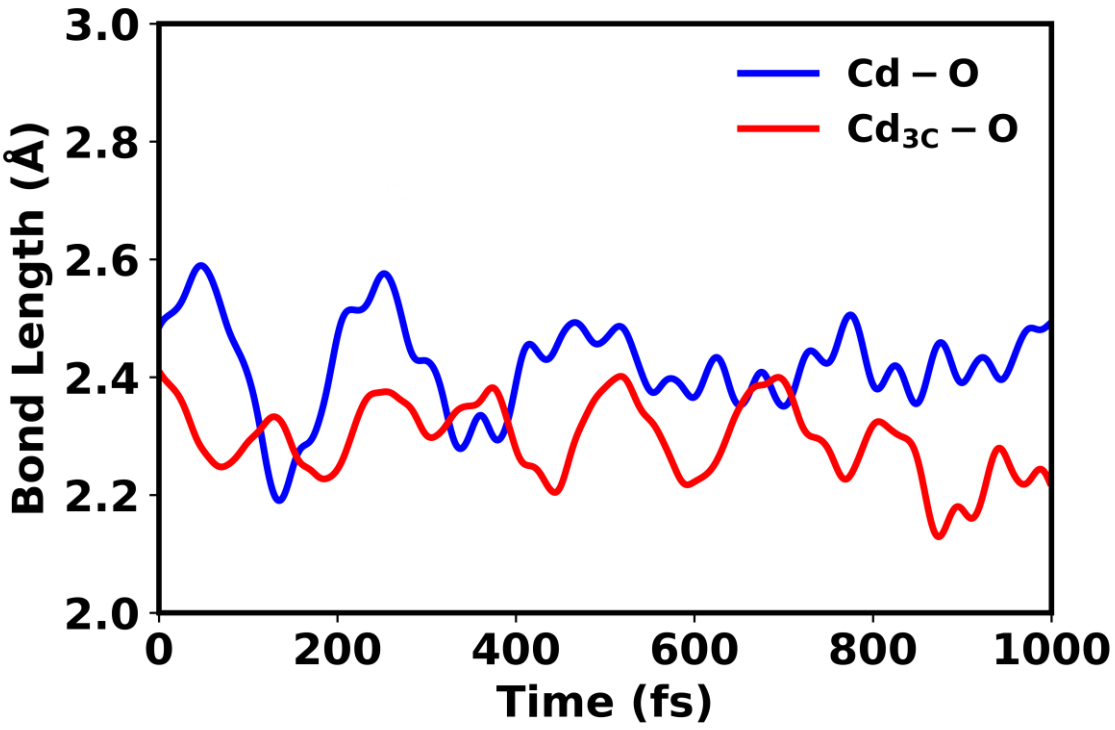

Figure S5: *The time evolution of Cd-O and Cd_{3c}-O bond length.*

Section S4: Hot Electron Trapping by Absorbate

Upon photoexcitation, hot electrons (HE) initially populate higher conduction band states before undergoing relaxation through two primary pathways: (a) charge transfer from higher-energy CBM states to the LUMO state of the molecule and (b) direct relaxation of HE to lower CB states without molecular state involvement.[6] We employ *ab initio* nonadiabatic molecular dynamics (NAMD) within the framework of time-dependent density functional theory (TDDFT) based on the Kohn-Sham (KS) formalism to investigate the dynamics of photogenerated electrons. The efficiency of hot electron (HE) extraction by the molecular state is governed by competing pathways. A key factor influencing hot electron dynamics is the nonadiabatic coupling (NAC), expressed as $d_{ij} = \frac{\langle \phi_i | \nabla_{\boldsymbol{R}} H | \phi_j \rangle \cdot \dot{\boldsymbol{R}}}{\varepsilon_i - \varepsilon_j}$

This relation highlights that NAC is directly proportional to the matrix elements of the electronic Hamiltonian and inversely proportional to the energy gap between the initial and final states. The strength of NAC quantifies the electron-phonon interactions over time. A higher NAC value between states signifies stronger electron-phonon coupling, leading to faster electronic transitions across states.[7,8] Our findings reveal that the charge relaxation within the QD CB and LUMO states occurs more rapidly than the relaxation between the higher CB states

and CBM. Figure 2c shows the calculated average NAC for HE cooling to LUMO state and CBM of QD.

Section S5: Impulsive two state Model

To investigate NO_3 dissociation induced by hot electron injection, we employ the Impulsive Two-State (I2S) model, a well-established approach for simulating electron-driven molecular reactions. In this framework, a single 1s electron is excited from the core-shell and transferred to the lowest unoccupied molecular orbital (LUMO) of NO_3.[9] This methodology has been successfully applied in previous studies on photochemical reaction dynamics.[10–12]

We use a canonical ensemble for ab initio molecular dynamics (AIMD) simulations. The I2S model simplifies electron-induced reaction simulations by describing the system's evolution across different potential energy surfaces (PES). The process begins with an excitation from the ground-state PES to an anionic excited-state PES* via electron injection. The system then evolves on PES* for a characteristic time interval, τ, acquiring additional energy and momentum. After this period, the system returns to the ground-state PES, where the accumulated energy facilitates bond dissociation by overcoming reaction barriers.

To examine the excitation dynamics within the I2S framework, we randomly selected a ground-state trajectory at 750 fs as the starting point for excitation. This trajectory then evolves under I2S conditions, allowing us to assess subsequent bond rearrangement.

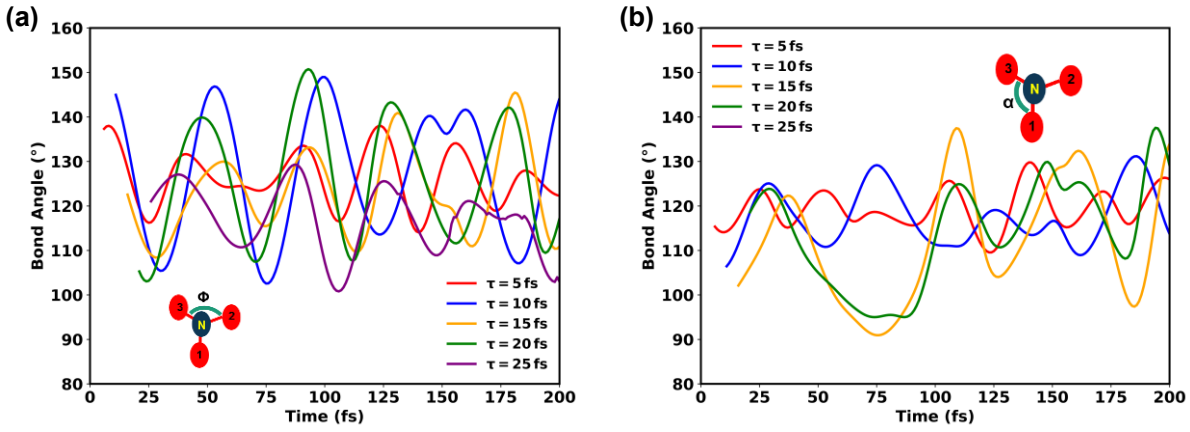

Figure S6: $\angle O_{Cd}{=}N{=}O_{Cd3c}$ **(a)** Φ and **(b)** α bond angle evolution over time at different lifetimes for initial configuration at 750 *fs* (τ = 5 *fs*, 10 *fs*, 15 *fs*, 20 *fs*, and 25 *fs*) of $NO_3^{\bullet-}$.

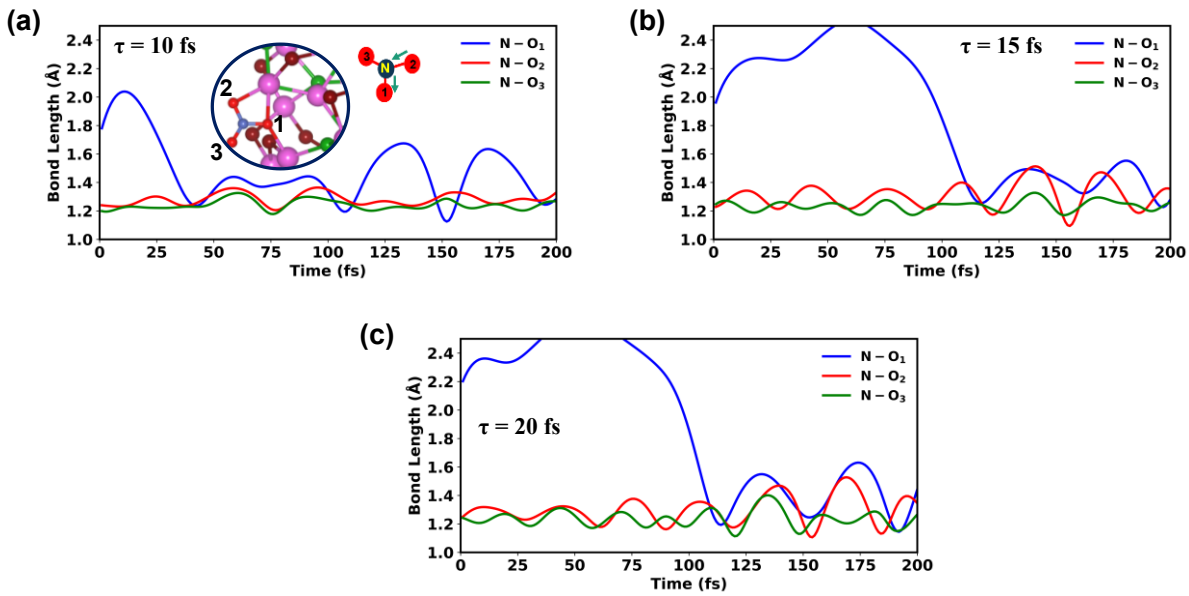

Figure S7: *N-O bond lengths $d_{N\text{-}O(1)}$, $d_{N\text{-}O(2)}$, and $d_{N\text{-}O(3)}$ evolution over time at* ***(a)*** *τ = 10 fs,* ***(b)*** *15 fs, and* ***(c)*** *20 fs.*

Different initial configuration:

To determine the minimum excitation time (τ) necessary for NO_3^- dissociation into NO_2^- + O*, we analyzed four randomly selected configurations from a thermodynamically equilibrated trajectory at 300 K. In each configuration, a single electron is excited to the LUMO of NO_3 and held there for varying durations, ranging from 5 to 25 *fs*. Following this excitation period, we monitored the system for 500 *fs* to assess whether dissociation occurred. We find that, for all selected configurations, NO_3^- dissociates into NO_2^- and O* at τ = 25 *fs*, as shown in Figure S8-S9.

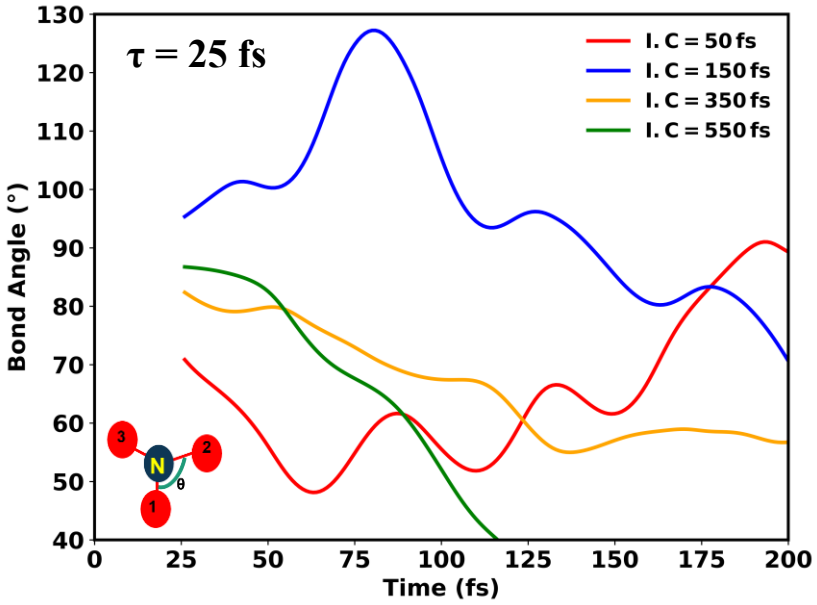

Figure S8: *$\angle O_{Cd}$=N=O_{Cd3c} (θ) bond angle evolution over time at τ = 25 fs for four different initial configurations (50 fs, 150 fs, 350 fs, and 550 fs).*

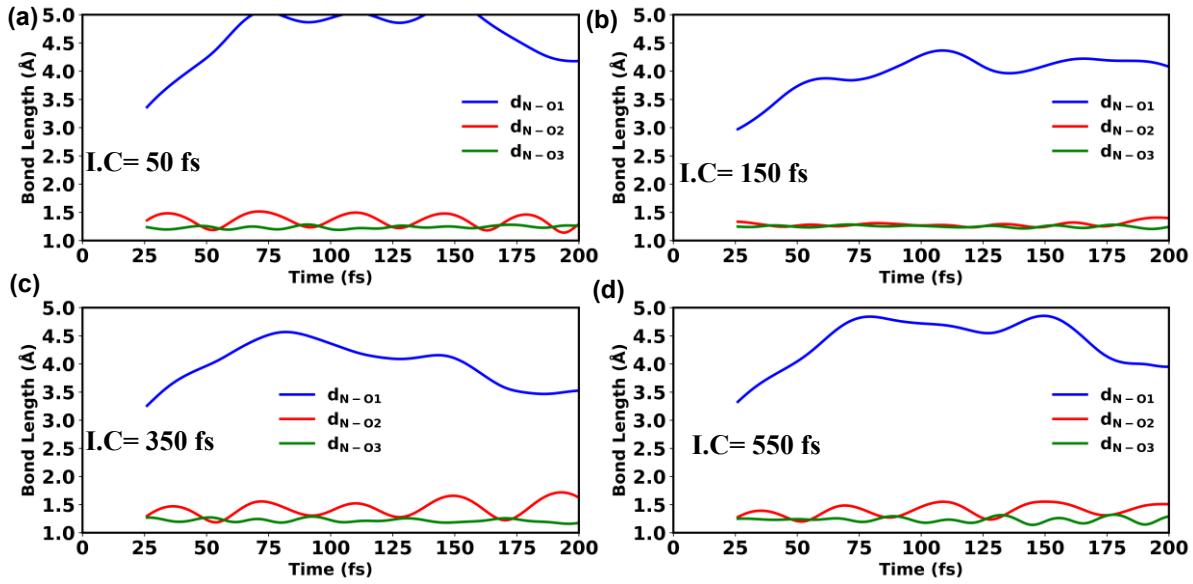

Figure S9: *N-O bond lengths $d_{N\text{-}O(1)}$, $d_{N\text{-}O(2)}$, and $d_{N\text{-}O(3)}$ evolution over time at τ = 25 fs for initial configurations (a) 50 fs, (b) 150 fs, (c) 350 fs, and (d) 550 fs.*

Section S6: Static Geometric and Electronic Details for QD-NO_2

To simulate the QD-NO_2 system, we take the final structure obtained after the dissociation of NO_3^- into NO_2^- + O*. This structure is then further optimized to model the QD-NO_2 configuration. The average Cd-Cl, Cd-Se, Cd-O, and N-O bond lengths are listed in Table S1.

Table S1:

QD-NO_2	***Bond length (Å)***
Cd-Se	2.78
Cd-Cl	2.58
Cd-O	2.43
N-O	1.27

The pDOS plot in Figure 4a shows that the LUMO of the unreacted NO_3 adsorbate remains energetically distant from the QD-NO_2 band edges and appears uncoupled, indicating its negligible influence during above-bandgap photoexcitation.

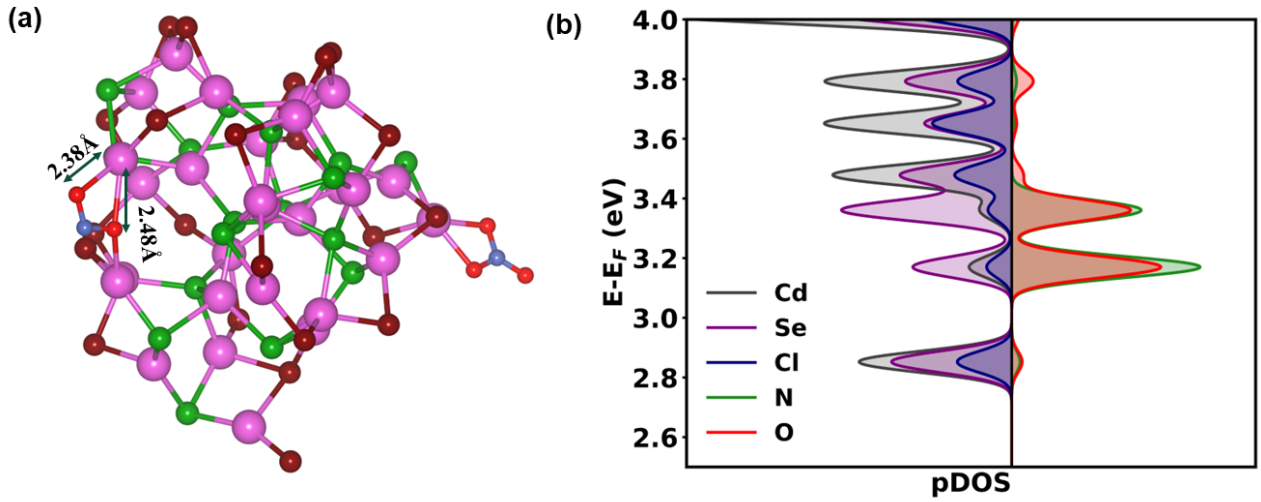

Figure S10: (a) *Optimized geometry of QD-NO_2 system. Color keys: pink (Cd), green (Se), maroon (Cl), red (O), and blue (N).* ***(b)*** *The pDOS plot using range-separated hybrid functionals (HSE06). The QD states are on the left, while the molecular LUMO states appear on the right.*

Section S7: Solvent Effects on the Molecular State

To evaluate the influence of solvation on the electronic structure of QD-NO_2, we compute the DOS using the VASPsol framework, considering both polar (water, ethanol) and non-polar (toluene) solvents. Figure S11 shows that the molecular state at CBM remains largely unaffected, with only minor energy shifts (~0.3-0.5 eV). The calculated NO_2^- binding energy to the QD surface in polar (water, ethanol) and non-polar solvents is in the range of -1.98 eV

to -2.04 eV, compared to -1.68 eV in the gas phase. This weak solvent dependence suggests that the electronic properties of QD-NO_2 are primarily governed by local bonding interactions. Given the minimal impact of solvation, we adopt a gas-phase model for further study. Additional computational details, including solvation model parameters, are provided in Section S3 (SI).

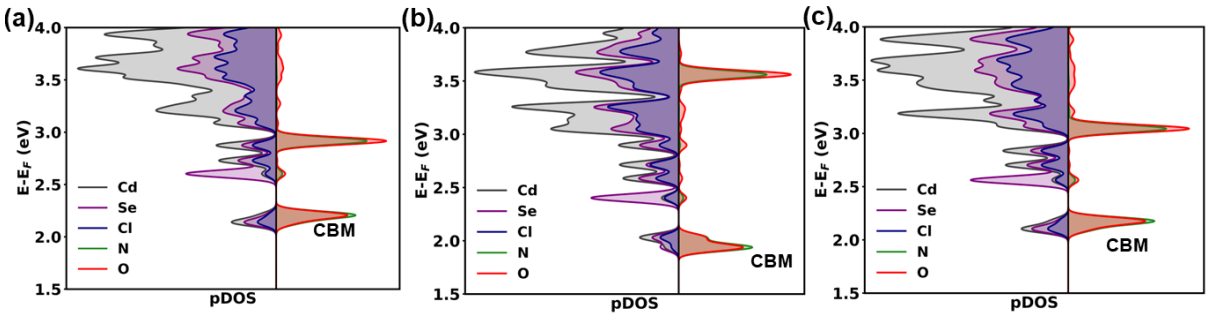

Figure S11: *The pDOS plot of the conduction band states of the QD-NO_2 system with solvent* ***(a)*** *water,* ***(b)*** *toluene, and* ***(c)*** *ethanol. The QD states are on the left, while the molecular LUMO states appear on the right.*

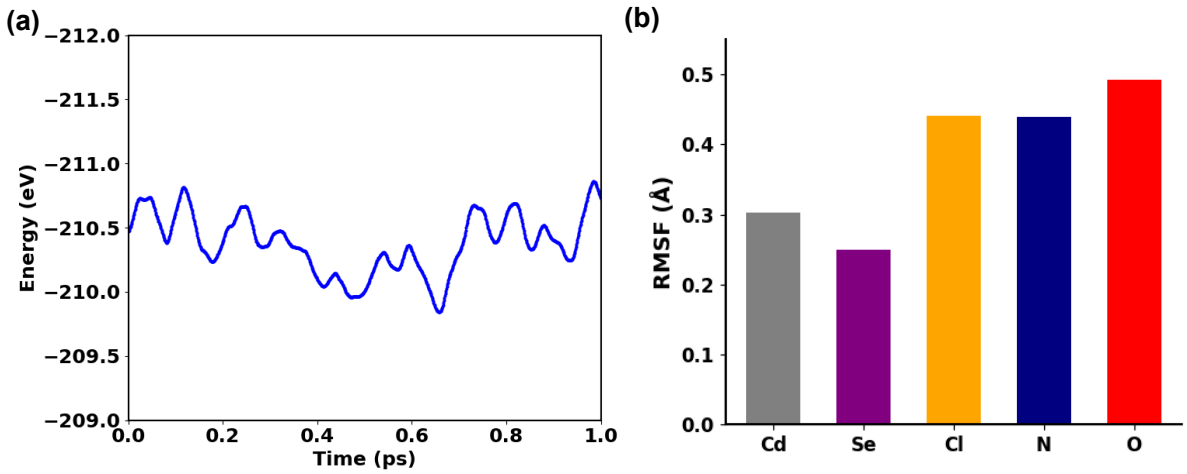

Figure S12:(a) *Potential energy curve for the QD-NO_2 system demonstrating equilibration at 300K for conducted AIMD simulations.* ***(b)*** *The root mean square fluctuations of individual elements of the $Cd_{28}Se_{17}Cl_{22}$-NO_2 QD system.*

Section S8: Hot carrier charge dynamics for QD-NO_2

To understand the mechanism governing electron retention in the NO_2 molecular state, we focus on the associated energy gap ΔE and phonon-induced NAC strengths. The smaller the energy gap, ΔE, the faster the carrier relaxation, while a larger average ΔE gap slows down carrier cooling.[13] We note that the large average ΔE (0.33 eV) gap between the higher CB QD states (CBM+2 and CBM+1) slows down the carrier cooling, while the smaller ΔE (0.16 eV) gap between CBM+1 and CBM state results in fast interfacial charge transfer.

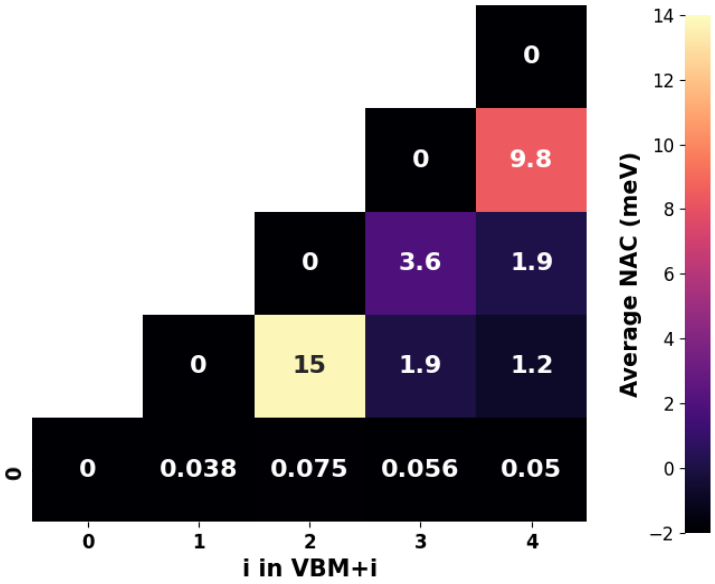

Figure S13: *Time-averaged NAC values between closely spaced QD states (CBM+1) and molecular LUMO state (CBM) and between the closest QD states.*

The second key factor is the NAC strengths of the involved electronic states. The higher the NAC values, the higher the nonradiative transition rate. Figure S13 shows the substantially higher time-averaged NAC values (15 meV) between the molecular LUMO state (CBM) and QD (CBM+1) results in ultrafast electron transfer in the NO_2 acceptor state. However, small NAC values between the CBM+2 and CBM+1 QD state (3.6 meV) slow carrier cooling from QD to the molecule state. The small NAC between the CBM (LUMO) and VBM (0.038 meV) prevents back-transfer of trapped HE from molecular state to QD.

The ability of NO_2 to capture hot electrons and drive reduction reactions highlights the broader potential of adsorbate-engineered quantum dots in photocatalysis. By strategically selecting adsorbates with favorable electronic properties, it may be possible to enhance the efficiency of solar-driven reduction processes.

Section S9: Impulsive two state for QD-NO_2 system

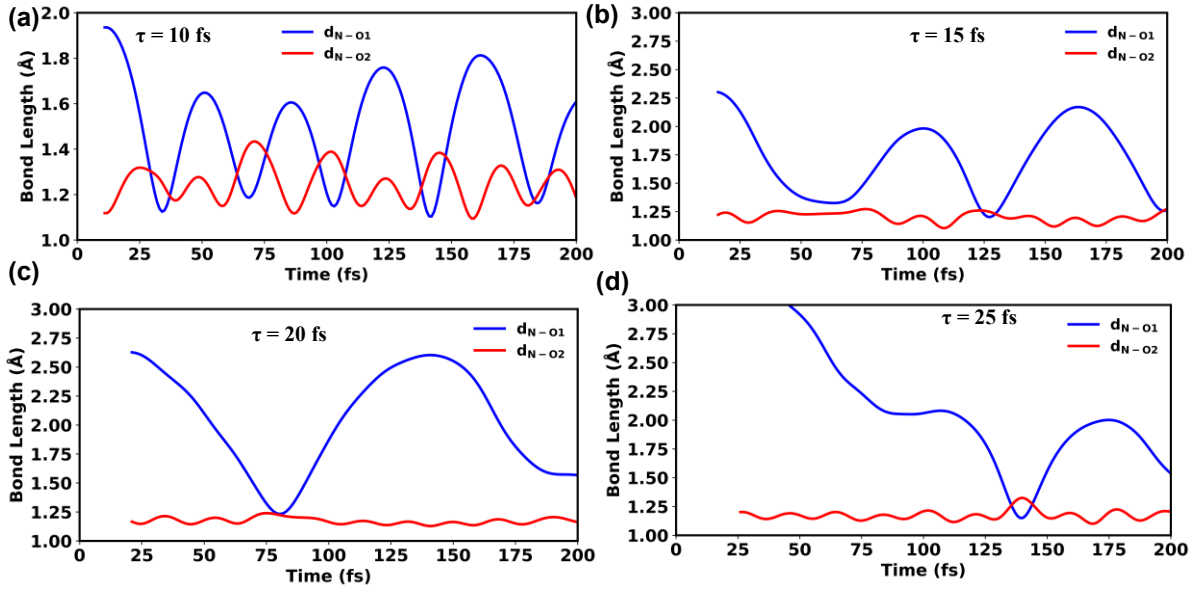

Figure S14: *N-O bond lengths $d_{N\text{-}O(1)}$ and $d_{N\text{-}O(2)}$ evolution over time at τ = 10 fs, 15 fs, 20 fs, and 25 fs.*

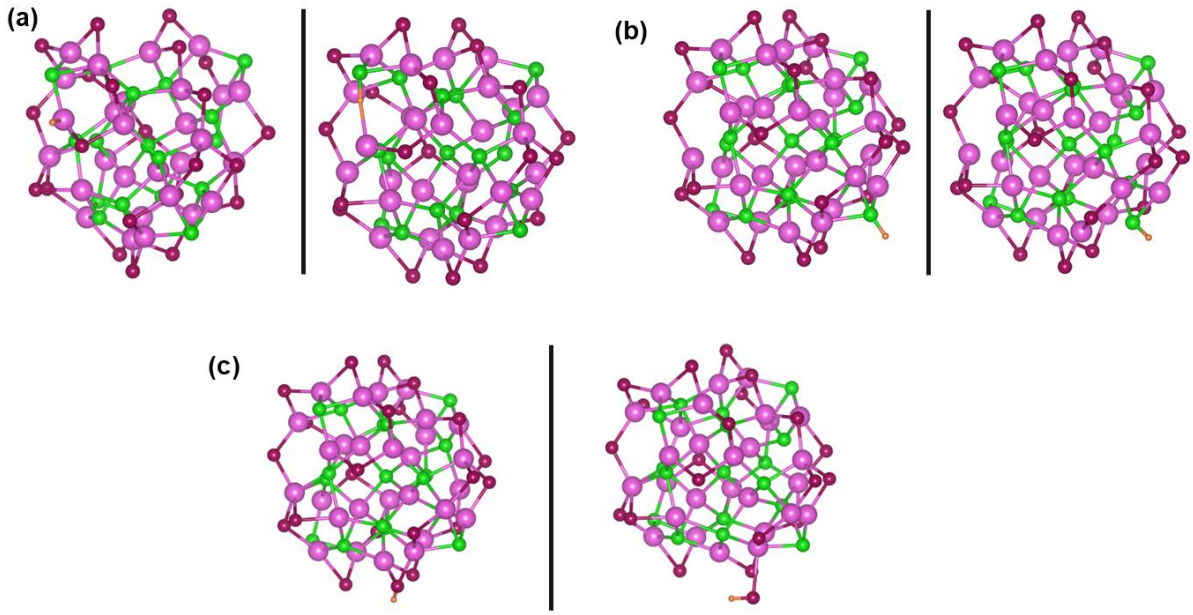

Figure S15:*Unoptimized geometry (left panel) and optimized geometry (right panel) of the hydrogen adsorbed on the* ***(a)*** *Cd-top site,* ***(b)*** *Se-top, and* ***(c)*** *Cl-top site of the $Cd_{28}Se_{17}Cl_{22}$ QD.*

Section S10: Computational Methodology

To evaluate the NO_3RR activity of catalysts, their adsorption-free energy (ΔG) is usually measured. Thus, ΔG can be defined as follows:

$$\Delta G = \Delta E + \Delta E_{ZPE} - T\Delta S \quad (1)$$

where, ΔG is the Gibbs free energy of nitrate adsorption, * represents the active site of the catalyst, ΔE is the adsorption energy, and ΔE_{ZPE} and ΔS are the zero-point energy and entropy difference of an atom between the adsorbed state and the gas-phase state.

The NAMD simulations follow a mixed quantum-classical framework, where the fast-moving electrons are treated quantum mechanically while heavier nuclei are described using classical mechanics.[14] All NAMD simulations in this study are performed within the time-dependent Kohn-Sham (TDKS) framework using the decoherence-induced surface hopping (DISH) approach.[15] The DISH algorithm is implemented within the classical path approximation (CPA) framework. The DISH method accounts for coherence loss in the electronic subsystem due to phonon interaction. The electron-hole recombination dynamics are analyzed using the LIBRA code.[16,17] This analysis involves 1000 geometries extracted from AIMD, with each geometry undergoing 100 stochastic realizations. To make the calculation manageable, we iterate the non-adiabatic Hamiltonian we compute for the 1 ps trajectory multiple times. This allows us to capture the charge recombination dynamics over a considerably longer duration.

Limitations of NAMD Simulations: The NAMD simulations performed in this work describe HC relaxation using a semi-classical fewest-switches surface-hopping (FSSH) scheme, where excited-state energies and non-adiabatic couplings are derived from TD-DFT. This framework inherently adopts a single-particle description and therefore does not capture many-body processes such as exciton formation or exciton renormalization, which require explicit electron-hole interactions beyond the mean-field approximation. In addition, Auger recombination and other multi-electron scattering channels are not included, as these processes involve higher-order electron–electron Coulomb interactions not accessible within standard FSSH.[18–20]

References

(1) Samanta, K.; Deswal, P.; Alam, S.; Bhati, M.; Ivanov, S. A.; Tretiak, S.; Ghosh, D. Ligand Controls Excited Charge Carrier Dynamics in Metal-Rich CdSe Quantum

Dots: Computational Insights. *ACS Nano* 2024. https://doi.org/10.1021/acsnano.4c05638.

(2) Fojt, J.; Rossi, T. P.; Kuisma, M.; Erhart, P. Hot-Carrier Transfer across a Nanoparticle–Molecule Junction: The Importance of Orbital Hybridization and Level Alignment. *Nano Lett* 2022, *22* (21), 8786–8792. https://doi.org/10.1021/acs.nanolett.2c02327.

(3) Mathew, K.; Sundararaman, R.; Letchworth-Weaver, K.; Arias, T. A.; Hennig, R. G. Implicit Solvation Model for Density-Functional Study of Nanocrystal Surfaces and Reaction Pathways. *J Chem Phys* 2014, *140* (8). https://doi.org/10.1063/1.4865107.

(4) Gauthier, J. A.; Dickens, C. F.; Chen, L. D.; Doyle, A. D.; Nørskov, J. K. Solvation Effects for Oxygen Evolution Reaction Catalysis on IrO 2 (110). *The Journal of Physical Chemistry C* 2017, *121* (21), 11455–11463. https://doi.org/10.1021/acs.jpcc.7b02383.

(5) Gray, C. M.; Saravanan, K.; Wang, G.; Keith, J. A. Quantifying Solvation Energies at Solid/Liquid Interfaces Using Continuum Solvation Methods. *Mol Simul* 2017, *43* (5–6), 420–427. https://doi.org/10.1080/08927022.2016.1273525.

(6) Zhou, Z.; Wu, Y.; He, J.; Frauenheim, T.; Prezhdo, O. V. Enhancing Extraction and Suppressing Cooling of Hot Electrons in Lead Halide Perovskites by Dipolar Surface Passivation. *J Am Chem Soc* 2024, *146* (43), 29905–29912. https://doi.org/10.1021/jacs.4c12042.

(7) Chu, W.; Zheng, Q.; Prezhdo, O. V.; Zhao, J.; Saidi, W. A. Low-Frequency Lattice Phonons in Halide Perovskites Explain High Defect Tolerance toward Electron-Hole Recombination. *Sci Adv* 2020, *6* (7). https://doi.org/10.1126/sciadv.aaw7453.

(8) Ghosh, D.; Acharya, D.; Pedesseau, L.; Katan, C.; Even, J.; Tretiak, S.; Neukirch, A. J. Charge Carrier Dynamics in Two-Dimensional Hybrid Perovskites: Dion–Jacobson *vs.* Ruddlesden–Popper Phases. *J Mater Chem A Mater* 2020, *8* (42), 22009–22022. https://doi.org/10.1039/D0TA07205B.

(9) Ji, W.; Lu, Z.-Y.; Gao, H. Electron Core-Hole Interaction and Its Induced Ionic Structural Relaxation in Molecular Systems under X-Ray Irradiation. *Phys Rev Lett* 2006, *97* (24), 246101. https://doi.org/10.1103/PhysRevLett.97.246101.

(10) Anggara, K.; Huang, K.; Leung, L.; Chatterjee, A.; Cheng, F.; Polanyi, J. C. Bond Selectivity in Electron-Induced Reaction Due to Directed Recoil on an Anisotropic Substrate. *Nat Commun* 2016, *7* (1), 13690. https://doi.org/10.1038/ncomms13690.

(11) Anggara, K.; Leung, L.; Timm, M. J.; Hu, Z.; Polanyi, J. C. Approaching the Forbidden Fruit of Reaction Dynamics: Aiming Reagent at Selected Impact Parameters. *Sci Adv* 2018, *4* (10). https://doi.org/10.1126/sciadv.aau2821.

(12) Huang, K.; Leung, L.; Lim, T.; Ning, Z.; Polanyi, J. C. Single-Electron Induces Double-Reaction by Charge Delocalization. *J Am Chem Soc* 2013, *135* (16), 6220–6225. https://doi.org/10.1021/ja400612c.

(13) Englman, R.; Jortner, J. The Energy Gap Law for Non-Radiative Decay in Large Molecules. *J Lumin* 1970, *1–2*, 134–142. https://doi.org/10.1016/0022-2313(70)90029-3.

(14) Craig, C. F.; Duncan, W. R.; Prezhdo, O. V. Trajectory Surface Hopping in the Time-Dependent Kohn-Sham Approach for Electron-Nuclear Dynamics. *Phys Rev Lett* 2005, *95* (16). https://doi.org/10.1103/PhysRevLett.95.163001.

(15) Jaeger, H. M.; Fischer, S.; Prezhdo, O. V. Decoherence-Induced Surface Hopping. *J Chem Phys* 2012, *137* (22). https://doi.org/10.1063/1.4757100.

(16) Shakiba, M.; Smith, B.; Li, W.; Dutra, M.; Jain, A.; Sun, X.; Garashchuk, S.; Akimov, A. Libra: A Modular Software Library for Quantum Nonadiabatic Dynamics. *Software Impacts* 2022, *14*, 100445. https://doi.org/10.1016/j.simpa.2022.100445.

(17) Akimov, A. V. Libra: An Open-Source “Methodology Discovery” Library for Quantum and Classical Dynamics Simulations. *J Comput Chem* 2016, *37* (17), 1626–1649. https://doi.org/10.1002/jcc.24367.

(18) Nelson, T. R.; White, A. J.; Bjorgaard, J. A.; Sifain, A. E.; Zhang, Y.; Nebgen, B.; Fernandez-Alberti, S.; Mozyrsky, D.; Roitberg, A. E.; Tretiak, S. Non-Adiabatic Excited-State Molecular Dynamics: Theory and Applications for Modeling Photophysics in Extended Molecular Materials. *Chem Rev* 2020, *120* (4), 2215–2287. https://doi.org/10.1021/acs.chemrev.9b00447.

(19) Zhou, G.; Lu, G.; Prezhdo, O. V. Modeling Auger Processes with Nonadiabatic Molecular Dynamics. *Nano Lett* 2021, *21* (1), 756–761. https://doi.org/10.1021/acs.nanolett.0c04442.

(20) Nelson, T.; Fernandez-Alberti, S.; Roitberg, A. E.; Tretiak, S. Nonadiabatic Excited-State Molecular Dynamics: Treatment of Electronic Decoherence. *J Chem Phys* 2013, *138* (22). https://doi.org/10.1063/1.4809568.